

Flow Field Analysis of a Detailed Road Vehicle Model Based on Numerical Data

Robin Placzek and Peter Scholz

Abstract The three-dimensional flow field of a detailed road vehicle model with focus on the importance of engine and underbody representation is studied. Further, issues of vortical flows are explored. Especially the presence of wheels and a detailed underbody has a major impact on the developing flow field. The numerical data provides the necessary insight into the main flow features such as the dominant wake structure typical for a bluff body. URANS simulations accounting for the inherent unsteadiness of the flow were performed in OpenFOAM® and were validated with experimental force and velocity field measurements using particle image velocimetry at a corresponding Reynolds number of 3 million. The results for the flow field showing a number of secondary effects interacting with the large areas of separated flow along and downstream of the model are discussed in detail. Another emphasis of the analysis is placed on the dependence of the wake structure on the characteristics of the underbody flow and the accuracy of the integral drag and lift coefficients. The study shows the particular importance of considering the impact of model simplifications on the global flow field of a road vehicle model.

1 Introduction

Higher standards for CO₂ emissions and fuel efficiency show the need for an improved aerodynamic performance of production cars. In order to enhance this performance, a more precise understanding of the global effects as well as the interaction with secondary effects is necessary. Due to the simplicity of most of the generic model configurations, results and trends are not necessarily transferable to detailed production cars [1] because more complex flow phenomena are not well captured. Heft et al.

R. Placzek (✉) · P. Scholz
Technische Universität Braunschweig, Hermann-Blenk-Straße 37,
38108 Braunschweig, Germany
e-mail: r.placzek@tu-bs.de

P. Scholz
e-mail: p.scholz@tu-bs.de

addressed this problem with the introduction of a realistic 1:2.5 scaled car model [2]. The DrivAer model is a detailed configuration based on two typical medium-class vehicles. Wojciak et al. [3] presented a numerical study on the DrivAer test case showing the capability of the open source package OpenFOAM® [4] to be used in unsteady vehicle aerodynamics. This issue had earlier been assessed by Islam et al. [5] who conducted DES simulations in OpenFOAM® for highly detailed production cars implying different flow phenomena. The presented study investigates the flow field of a detailed road vehicle model and the impact of simplified engine and underbody representation.

2 Model Geometry and Computational Domain

This study presents a numerical and experimentally validated analysis of the three-dimensional flow field of a 1:4 road vehicle model of the Volkswagen up!. The model, presented in Fig. 1, is equipped with side mirrors, wheels and wheel houses, as well as a rear spoiler. The detailed underbody features the front spoiler, a simplified representation of the front axle (red box), exhaust piping, tank, rear axle including suspension and the spare wheel recess. This set-up defines the reference configuration.

The second configuration, that will be a subject of discussion, features an additional front cover inserted as a substitute for the missing engine compartment which is shown in Fig. 2 on the right side and highlighted in green (A). It basically just seals

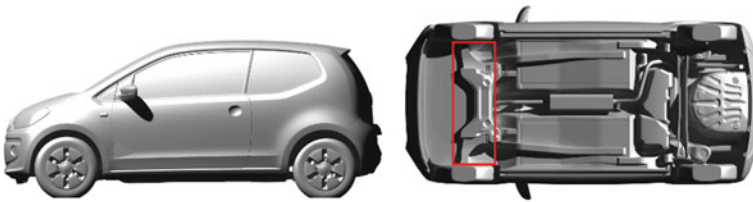


Fig. 1 Reference configuration of the 1:4 scale road vehicle model, *left* side view, *right* underbody

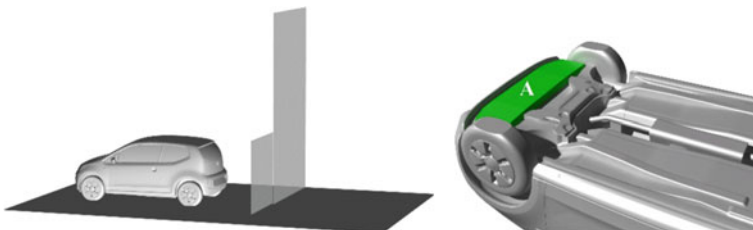


Fig. 2 *Left* position of the SPIV measurement plane (small window on the left) and the numerical slice for comparison, *right* front cover (A) applied to the reference configuration

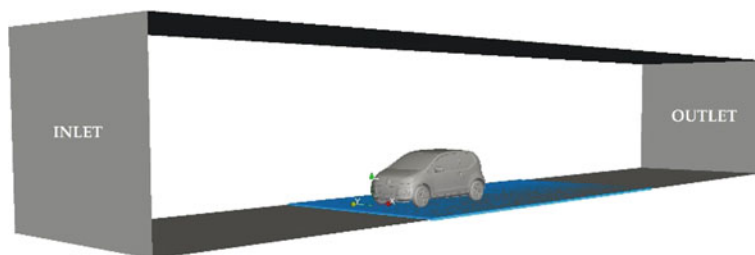


Fig. 3 Computational domain showing the inlet/outlet and the upper half of the track (colored in blue) [6]

up the cavity between the front spoiler and the front axle leaving only a narrow gap between these edges. Cooling-air flow was not simulated.

The freestream velocity was set to 50 m/s with a corresponding Reynolds number of $Re = 3.0 \times 10^6$ based on the model's chord-length $c = 0.885\text{m}$. The numerical domain represents the in-house wind tunnel with a closed $1.3 \times 1.3\text{m}^2$ test section. A thin ground board featuring an elliptical nose was installed as a track to minimize the effect of the evolving boundary layer underneath the vehicle. This type of ground simulation is considered to be adequate because the underbody flow is dominated by the distinctive displacement effect of the vehicle [1]. Thus the height of the numerical domain based on the model's height h is $z/h = 3.0$, where the upper half of the non-moving ground board ($z/h = 0.02$, colored in blue) is represented. The lower half of the ground board as well as the flow passing underneath are not part of the simulation. The width based on the model's width b is $y/b = 2.7$. Domain walls, except the ground board, are treated as slip-walls. The front edge of the model is placed at $x/c = 0.0$, the inlet is located at $x/c = -2.5$ and the outlet at $x/c = 5.4$ (Fig. 3).

Wind tunnel experiments were conducted for validation of the numerical simulation featuring force measurements with a six-component force transducer, static pressure measurements, oil visualization and stereoscopic particle image velocimetry (SPIV) within the wake of the model. The x -position of the SPIV plane at $x/c = 1.35$ within the test section is shown in Fig. 2. It also shows a YZ -slice of the lateral and vertical expansion of the numerical domain. Refer to [6] for a more detailed description of the experimental setup and the 3C2D-SPIV measurements of this test case. The rotation of the wheels is not represented, neither in the wind tunnel experiments nor in the numerical simulation.

3 Numerical Approach

The numerical simulations were conducted within the open source OpenFOAM® software environment (Version 2.1.1.) [4]. Due to the inherent unsteadiness of the flow the incompressible flow solver *pisoFoam* [7], based on the PISO-algorithm [8], was applied solving the unsteady Reynolds-averaged Navier-Stokes (URANS)

equations. The linear GAMG (generalized geometric-algebraic multi-grid solver) with a Gauss-Seidel smoother is used for solving the pressure equation. The U, k and omega equations are solved with a smooth solver applying Gauss-Seidel smoothing. A first-order Euler scheme is used for temporal discretization. For spatial discretization a second-order upwind scheme is used for convective momentum fluxes and a first order upwind scheme for convective turbulent fluxes. Diffusive fluxes are computed with a central scheme [9]. For turbulence modelling the two equation k- ω -SST model [10] linked with wall functions is applied. Due to the wide range of dimensionless wall distance values varying between $1 < y^+ < 200$, a hybrid wall function is used for the turbulent kinematic viscosity employing the continuous Spalding law of the wall. High y^+ values appear within regions of highly accelerated flow, for instance along the acceleration of the flow over the hood, the roof and the A-pillars as well as around the front shoulders of the tires or side mirrors. Thus the hybrid wall function approach is valid for the logarithmic law region as well as for the viscous sublayer, where exact boundary conditions are used. A velocity inlet with zero pressure gradient and a fixed pressure outlet are set as boundary conditions [11]. The final unstructured mesh with 16.3 Mio points was generated using the meshing utility *snappyHexMesh* based on a background mesh created with *blockMesh* [5]. The study for mesh convergence was conducted by modifying the mesh density of the background meshes with the same factor n in all directions to reach convergence for the drag and lift coefficient. The size of the finest mesh tested was 40.7 Mio cells, where the difference in results, as compared to the 16 Mio mesh, are much less than the difference due to the case variations that will be discussed herein. Thus, the results can be considered to be independent of the mesh. To improve stability and convergence rate the *potentialFoam* solver was used to initialize the internal field. The parallel computation then was run for 1 s real time with a time step of 1.0×10^{-5} s averaging the field every time step for the last 0.5 s real time (also refer to [3]).

4 Results

The results of the simulated time-averaged flow field of the reference configuration provide an insight into the flow characteristics. To begin with, Fig. 4 gives a general impression of the flow field showing the pressure distribution along the surface of the model and the track. The stagnation area at the radiator grill (A) along with a region with a pressure larger than $c_p = 0$ on the track in front of the model (B) is clearly visible. Also the acceleration of the flow passing the hood (C) and the roof top (D) as well as after the front spoiler below the front axle (E) is indicated by $c_p < 0$. The upper side part downstream of the rear windows (F) also shows a low value for c_p . This indicates that the flow is pulling inwards into the wake and inducing a downwash behind the model. This behavior has also been observed by Wojciak et al. [3] for a RANS computation with the SST turbulence model. The isosurface at a non-dimensional x-velocity of $u/U = 0$ shows a large region of recirculating flow (G) within the wake of the model. The two nearly symmetrical structures (H) sitting

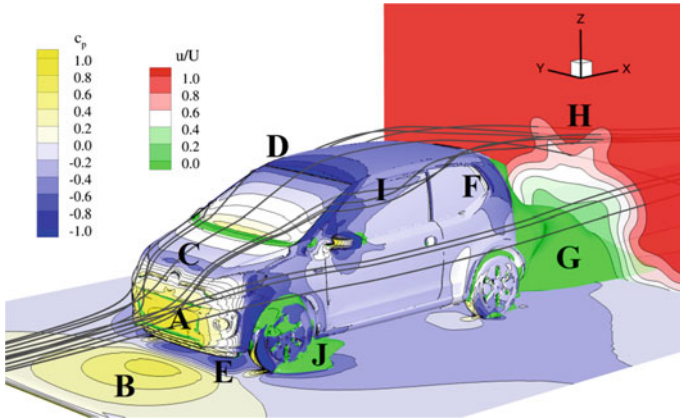


Fig. 4 Surface pressure distribution on the model and the ground and visualization with streamlines, freestream velocity component at $x/c = 1.35$ and isosurface at $u/U = 0$

above the wake, illustrated with a YZ-slice at $x/c = 1.35$, can be traced back to the A-pillar vortex (I) visualized with streamlines. With respect to the simplifications like the non-moving floor and wheels as well as the missing cooling-air flow, the extent of the separation close to the front tire (J) indicates that for this configuration the flow is passing the front tires with a high side angle.

Figure 5 shows the visualization of flow features for the reference case using different x-vorticity values. In the top picture with a side view of the model, isosurfaces

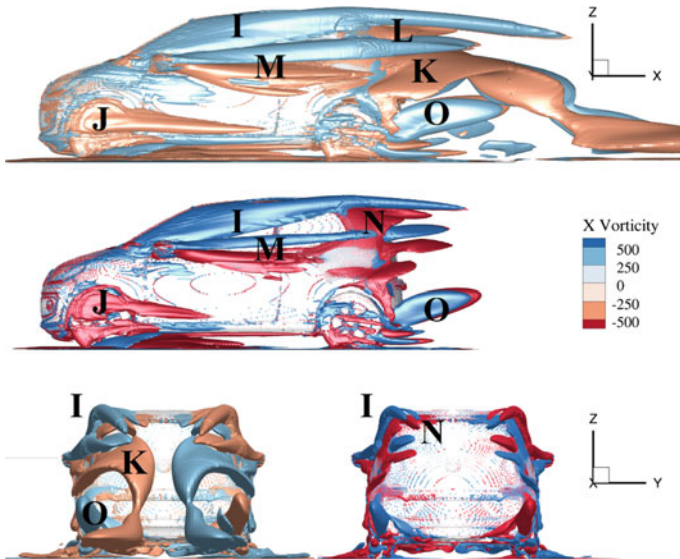


Fig. 5 Isosurfaces of the mean x-vorticity for the reference configuration

are generated for an x -vorticity of $\pm 250 \text{ s}^{-1}$. The same isosurfaces are shown for the rear view in the bottom-left picture. In the middle, isosurfaces are generated just for a higher x -vorticity of $\pm 500 \text{ s}^{-1}$ in order to emphasize the vortex cores and trajectories. Two large longitudinal structures (K) appear downstream of the base and give another hint on the downwash within the wake. Due to their low rotational motion they do not show up in the high vorticity plot. The separation behind the front tire (J) also seems to contain only a low magnitude of vorticity since it dissolves quite fast traveling downstream. By contrast the upper side part region in the back (L) features a complex vortex system. On the one hand there is an interaction of the A-pillar vortex (I) with the two vortices underneath (M) with contrary rotation, which can be traced back to the side mirror separation. On the other hand there is another small vortex (N) at the trailing edge of the top corner that forms due to a small separation at the intersection of the rear spoiler and the side trailing edge. Because of the separation behind the rear wheels the underbody flow also generates a small longitudinal structure (O).

The comparison of the pressure distribution for the center plane in Fig. 6 shows how the integration of the front cover leads to a strong suction peak (W) downstream of the front spoiler compared to the reference configuration (V), where the pressure level is nearly constant for the front part (three pressure taps). For the reference configuration there is a little offset between CFD and the experiment at the lower front part.

A comparison of the mean cross-flow velocity field between the experimental SPIV data and the numerical data for the reference configuration is shown in the top picture of Fig. 7 at $x/c = 1.35$. The simulation as well as the PIV data shows the large separated area with the distinctive backflow close to the bottom (P). The residuals (H) of the A-pillar vortices are also visible [6]. However the simulation appears to slightly overpredict the downwash into wake. Another sign for this conclusion is the numerical overprediction of the lift coefficient by 0.155. With a deviation of 5 drag counts, equal to 1.2%, the numerical value of 0.415 matches the experimental drag coefficient of 0.410 already quite well. The bottom picture of Fig. 7 shows the comparison of the experiment and the simulation for the configuration with the integrated front cover. Again the A-pillar vortex residuals (H) appear, but the characteristics of the main wake structure have changed. The large backflow region (P) of the reference configuration is no longer present.

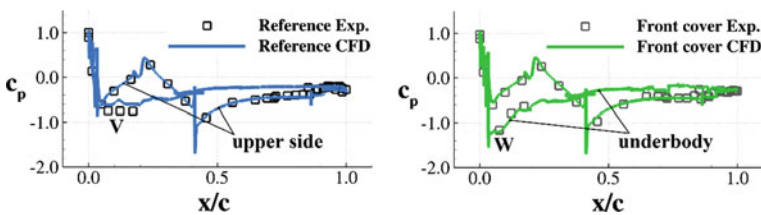


Fig. 6 Pressure distribution along the center plane $y = 0$ for the reference configuration and the configuration with the front cover applied

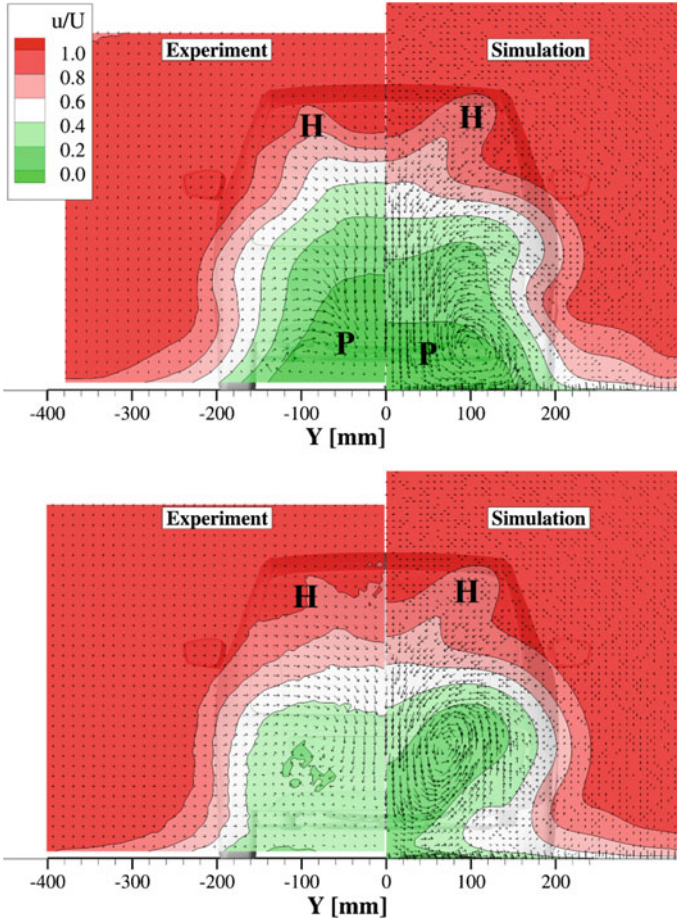


Fig. 7 Comparison of the freestream velocity component and the mean cross-flow direction measured with SPIV (every 2nd vector shown) and predicted by CFD (every 8th vector shown) at $x/c = 1.35$, *top* reference configuration, *bottom* front cover applied to the reference configuration

Table 1 Comparison of integral coefficients

CONFIGURATION	Num. C_D	Exp. C_D	ΔC_D	Num. C_L	Exp. C_L	ΔC_L
Reference	0.415	0.410	0.005	0.190	0.035	0.155
Front cover	0.409	0.410	0.001	0.087	0.062	0.025

Instead the introduction of the front cover leads to an improved agreement between the numerical simulation and the experimental measurement. The drag coefficient now is only 1 drag count off. Also the prediction of the lift coefficient has improved showing a difference of only 0.025. Obviously the configuration with the front cover is less sensitive to numerical inaccuracy. Table 1 gives an overview of the integral

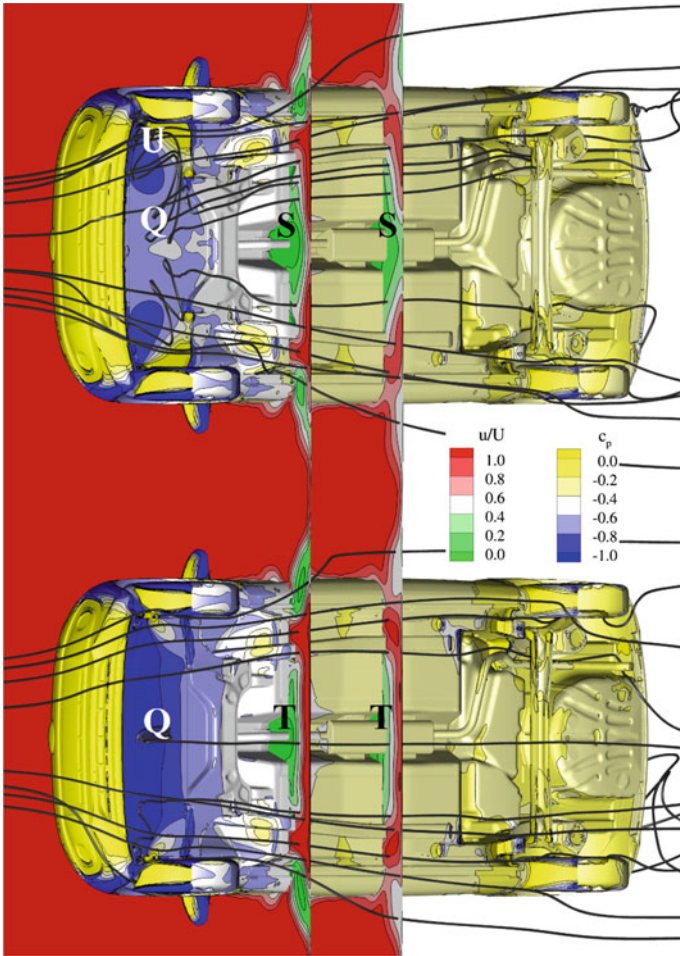


Fig. 8 Visualization of the underbody flow using streamlines, the surface pressure distribution and the freestream velocity component in two slices positioned at $x/c = 0.33$ and $x/c = 0.5$, *top* reference configuration, *bottom* front cover applied to the reference configuration

drag and lift coefficients for the reference configuration and the configuration with the front cover applied.

To analyze this behavior and to point out how the front cover, which is integrated upstream, affects the wake structure, Fig. 8 shows a visualization of the underbody flow for both configurations including two YZ-slices positioned at $x/c = 0.33$ and $x/c = 0.5$. The contour plot displays the pressure coefficient on the model surface. Comparing the two plots, a significant discrepancy with a lower c_p in the vicinity of the front cover (Q) can be noted. This difference can be explained by looking at the reference case. Downstream of the spoiler the flow detaches and a large separation bubble forms in the middle underneath the front axle (R). The rotation

of the streamlines give an idea of the bubble. Primarily this is attributed to the large forward facing step implied by the front axle (also refer to Fig. 1, highlighted with the box) where another stagnation area appears (U). The bubble creates a blockage causing the flow to divert towards the sides. This is also indicated by the streamlines that are deflected. The velocity profiles of the two slices show the asymmetry of the momentum distribution (S) downstream of the separated region. The simplified front axle and the missing engine compartment unfortunately favor the large separation bubble. When the front cover is applied the separation bubble is suppressed and the velocity profile is symmetrical (T). Also the diversion of the flow, represented by the streamlines, is less pronounced for this configuration.

The problem of massive separation around the front axle does not exist for a full-scale car because on the one hand there is the engine flow and on the other hand because the real axle allows the flow to pass it above and underneath. Therefore the implementation of the front cover at the model, although it is not a geometrical representation of the full size car, features a flow, that better reflects the underbody aerodynamics of a real configuration.

5 Conclusion

In this study, the three-dimensional flow field of a detailed road vehicle model has been investigated. It was shown how geometrical details lead to a complex flow field. The study also proves the capability of the OpenFOAM® URANS simulation to accurately predict the interaction of the numerous flow features and the integral coefficients for an unsteady incompressible flow. This has been validated with experimental force and stereoscopic PIV measurements. Another aim was the investigation of the impact of a simplified engine and underbody representation. It was shown how model simplifications like the engine compartment can lead to non-negligible model sensitivities which influence the global flow field. Below the engine compartment a front cover can be applied to establish a flow that is much closer to the one of a real configuration, even though it is not a geometrical representation of the simplified parts. This improves the transferability of results obtained for a wind tunnel model to a full scale car.

Acknowledgments The authors gratefully acknowledge the support for this research by Volkswagen AG, with special thanks to Dr. Carsten Othmer.

References

1. Hucho, W.-H.: Windkanäle. In: Hucho, W.-H. (ed.) *Aerodynamik des Automobils*. Vieweg+Teubner-Verlag, Wiesbaden (2005)
2. Heft, A.I., Indinger, T., Adams, N.A.: Introduction of a new realistic generic car model for aerodynamic investigations. SAE Technical Paper 2012-01-0168 (2012)

3. Wojciak, J., Schnepf, B., Indinger, T., Adams, N.A.: Study on the capability of an open source CFD software for unsteady vehicle aerodynamics. *SAE Int. J. Commer. Veh.* **5**(1) (2012)
4. <http://www.openfoam.com>
5. Islam, M., Decker, F., de Villiers, E., Jackson, A., Gines, J., Grahs, T., Gitt-Gehrke, A., Comas i Font, J.: Application of detached-eddy simulation for automotive aerodynamics development. SAE Technical Paper 2009-01-0333 (2009)
6. Placzek, R., Scholz, P., Othmer, C.: An analysis of drag force components and structures in the wake of a detailed road vehicle model by means of SPIV. In: Proceedings of the 17th International Symposium on Applications of Laser Techniques to Fluid Mechanics, Lisbon, Portugal (2014)
7. Jasak, H.: Error analysis and estimation for the finite volume method with applications to fluid flows. Ph.D. Thesis, Imperial College, London (1996)
8. Issa, R.I.: Solution of implicitly discretized fluid flow equations by operator-splitting. *J. Comput. Phys.* **62**, 40–65 (1986)
9. Ferziger, J.H., Peric, M.: *Computational Methods for Fluid Dynamics*, 3rd edn. Springer, Berlin (2002)
10. Menter, F., Esch, T.: Elements of industrial heat transfer predictions. In: Proceedings of the 16th Brazilian Congress of Mechanical Engineering. ISBN 85-85769-06-6 (2001)
11. Gagnon, L., Rischard, M.J.: Parallel CFD of a prototype car with OpenFOAM. In: Proceedings of the 5th OpenFOAM Workshop, Chalmers, Gothenburg, Sweden, 21–24 June 2010